Colloidal Polymerization of Polymer-Coated Ferromagnetic Nanoparticles into Cobalt Oxide Nanowires

Pei Yuin Keng,[†] Bo Yun Kim,[†] In-Bo Shim,[‡] Rabindra Sahoo,[†] Peter E. Veneman,[†] Neal R. Armstrong,[†] Heemin Yoo,[†] Jeanne E. Pemberton,[†] Mathew M. Bull,[†] Jared J. Griebel,[†] Erin L. Ratcliff,[†] Kenneth G. Nebesny,[†] and Jeffrey Pyun[†,*]

[†]Department of Chemistry, University of Arizona, Tucson, Arizona 85721, and [‡]Department of Nano and Electronic Physics, Kookmin University, Seoul, Korea 136-702

ABSTRACT The preparation of polystyrene-coated cobalt oxide nanowires is reported *via* the colloidal polymerization of polymer-coated ferromagnetic cobalt nanoparticles (PS-CoNPs). Using a combination of dipolar nanoparticle assembly and a solution oxidation of preorganized metallic colloids, interconnected nanoparticles of cobalt oxide spanning micrometers in length were prepared. The colloidal polymerization of PS-CoNPs into cobalt oxide (CoO and Co_3O_4) nanowires was achieved by bubbling O_2 into PS-CoNP dispersions in 1,2-dichlorobenzene at 175 °C. Calcination of thin films of PS-coated cobalt oxide nanowires afforded Co_3O_4 metal oxide materials. Transmission electron microscopy (TEM) revealed the formation of interconnected nanoparticles of cobalt oxide with hollow inclusions, arising from a combination of dipolar assembly of PS-CoNPs and the nanoscale Kirkendall effect in the oxidation reaction. Using a wide range of spectroscopic and electrochemical characterization techniques, we demonstrate that cobalt oxide nanowires prepared *via* this novel methodology were electroactive with potential applications as nanostructured electrodes for energy storage.

KEYWORDS: magnetic nanoparticles · cobalt nanoparticles · ferromagnetic nanoparticles · cobalt oxide nanowires · Co_3O_4 nanowires · electrochemistry · Raman spectroscopy · photoelectron spectroscopy · magnetic assembly · dipolar assembly · colloidal polymerization

The preparation of nanostructured conductive metal oxides is an important technological challenge toward the creation of improved materials for energy storage and (photo)electrochemical catalysis for water splitting.[1−4] Semiconductor metal oxides, such as, TiO_2, RuO_2, Fe_2O_3, and Co_3O_4, have been widely explored as electrode materials in a number of energy related applications in photovoltaics, (photo)electrolytic water splitting, batteries, and supercapacitors.[5−8] Cobalt oxides, such as, cobalt cobaltite (Co_3O_4) have been widely investigated as electrode materials for lithium batteries, catalysts for water reduction, and carbon monoxide oxidation, electrochromic materials, and gas sensors.[9−16]

The preparation of nanostructured Co_3O_4 has been explored as a route to enhance the electrochemical and catalytic properties of these materials *via* both an increase in the electroactive surface of the electrode films and improved charge transport from nanoscale ordering.[11,12,14] Co_3O_4 thin films have been prepared by numerous routes, including electrodeposition and sputtering techniques.[17−25] Colloidal forms of Co_3O_4 have been synthesized using solvothermal/hydrothermal techniques to synthesize well-defined nanocrystals and hollow nanospheres.[26−40] Nanostructured mesoporous materials have also been prepared using sol−gel precipitation in the presence of either hard, or soft templates.[41−45] One-dimensional (1-D) Co_3O_4 nanomaterials have also recently been prepared using a variety of different approaches, namely, sol−gel precipitation,[13,15] oxidation of metallic cobalt (Co) foils,[46] hydrothermal processes,[47,48] polyol reduction,[49] and electrospinning.[50−52] Despite these numerous advances, the preparation of high aspect ratio 1-D Co_3O_4 nanowires, without the use of structure-directing templates, remains an important synthetic challenge in gram-scale quantities.

The use of nanoparticle precursors as chemical reagents has recently gained significant attention as a novel approach to prepare hierarchically complex materials. Recent examples of using nanoparticles as "colloidal molecules" have been reported for the preparation of novel colloidal crystals,[53] well-defined clusters,[54] supramolecular amphiphiles,[55] and mesoscopic polymer chains.[56,57] The assembly of nanoparticles into one-dimensional (1-D) nanomaterials has been achieved using a number of approaches, notably, selective ligand chemistry on Au, or iron oxide NPs[58−61] and chemical linking of dipolar colloids.[62−78] An elegant demonstration of using nanoparticles as reagents in chemical reactions has

*Address correspondence to jpyun@email.arizona.edu.

Received for review May 11, 2009 and accepted September 8, 2009.

Published online October 2, 2009.
10.1021/nn900483w CCC: $40.75

been the preparation of hollow semiconductor colloids *via* the nanoscale Kirkendall effect. Alivisatos *et al.* reported the preparation of discrete hollow cobalt oxide, or cobalt sulfide NPs by the oxidation/sulfidation of dispersed superparamagnetic CoNP precursors.[79,80] Hollow cobalt selenide ($CoSe_2$) nanowires have also been prepared by the combination of dipolar NP assembly[81] and the nanoscale Kirkendall effect using ferromagnetic CoNPs passivated with small molecule surfactants.[71] Using these design principles we have developed a facile synthetic methodology to use ferromagnetic nanoparticles as dipolar precursors to prepare cobalt oxide nanowires.

Herein, we report the synthesis and characterization of hollow cobalt oxide nanowires *via* the "colloidal polymerization" of ferromagnetic polystyrene coated cobalt nanoparticles (PS-CoNPs). The colloidal polymerization process is described as a combination of dipolar nanoparticle assembly and a chemical reaction converting colloidal precursors into a fused 1-D material. In this report, cobalt oxide nanowires were formed by the magnetic preorganization of metallic PS-CoNPs into 1-D mesostructures and subsequent oxidation of the assembled colloids. This process is reminiscent of the step-growth polymerization of A−B small molecule monomers to form macromolecules, as dipolar metallic PS-CoNPs were employed as "colloidal monomers" to form interconnected 1-D mesostructures and is a mesoscale variation of supramolecular polymerization.[82−85] This particular approach enabled the preparation of very fine cobalt oxide nanowires that were passivated with a polymeric steric layer that imparted colloidal stability when dispersed in organic media. Furthermore, calcination of the polymer-coated cobalt oxide nanowires was achieved along with spectroscopic, electrical, and electrochemical characterization of these nanomaterials, which confirmed for the first time the viability of this synthetic methodology (*i.e.*, colloidal polymerization *via* dipolar assembly and the Kirkendall effect) to form electroactive materials.

RESULTS AND DISCUSSION

Colloidal Polymerization of Ferromagnetic Metallic Cobalt Nanoparticles into 1-D Cobalt Oxide Nanostructures. The synthesis of PS-coated cobalt oxide nanowires was conducted by bubbling O_2 into 1,2-dichlorobenzene (DCB) dispersions of ferromagnetic PS-CoNPs at 175 °C for varying reaction times in the absence of an external magnetic field (*i.e.*, zero field conditions) (Scheme 1). Well-defined ferromagnetic PS-CoNPs were prepared using amine end-functional polystyrene surfactants in the thermolysis of dicobaltoctacarbonyl ($Co_2(CO)_8$), as reported previously. Amine-terminated PS surfactants were synthesized using controlled polymerizations,[86−88] namely, atom transfer radical polymerization (ATRP)[89] which enabled precise control of polymer molar mass, composition, and functional group placement. TEM images of

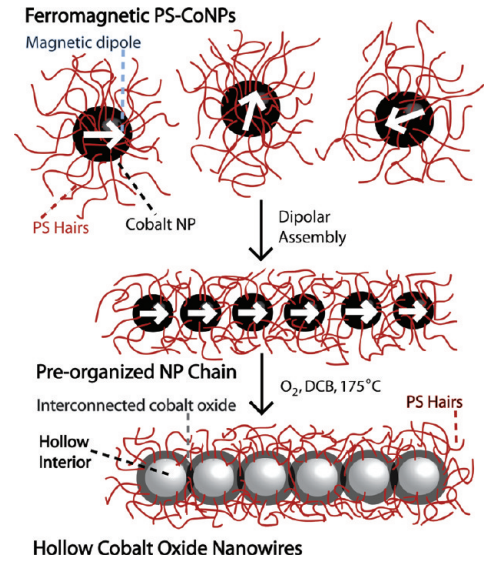

Scheme 1. Colloidal Polymerization of Ferromagnetic PS-CoNPs into Cobalt Oxide Nanowires

ferromagnetic PS-CoNPs (Figure 1a,b) confirmed the preparation of uniformly sized colloids ($D = 20 \pm 2.4$ nm) that self-assembled into 1-D mesostructures from interparticle dipolar associations when deposited onto a supporting substrate in zero field. We previously reported that our synthetic methods for PS-CoNPs enabled the preparation of well-defined colloidal building blocks in appreciable quantities (~800 mg per reaction) and were easily redispersible in various organic solvents (*e.g.*, toluene, tetrahydrofuran, methylene chloride) due to the polymer coating passivating the magnetic colloid. These synthetic conditions for this report were further optimized to enable nearly doubling of the yield of ferromagnetic PS-CoNPs (yield = 1.53 g) that were also readily stored as powders and redispersed into organic solvents.

In the conversion of PS-CoNPs into PS-coated cobalt oxide nanowires, the oxidation reaction was carried out by bubbling oxygen into the PS-CoNP ferrofluid at elevated temperature ($T = 175$ °C). The use of ferromagnetic PS-CoNPs was essential to the formation of cobalt oxide nanowires under zero field conditions, as superparamagnetic CoNPs were unable to polymerize due to the absence of a permanent dipole above cryogenic temperatures.[71] A striking feature of 1-D mesostructures formed *via* this colloidal polymerization was the presence of hollow inclusions in every nanoparticle repeating unit within cobalt oxide nanowires. These hollow inclusions were formed in the oxidation reaction due to a *nonuniform* diffusion and reaction of O_2 with Co atoms throughout the metallic NP. Under these conditions, oxidation of the NP was confined to the outer shell, resulting in depletion of Co atoms from the colloidal core to satisfy the valency of O atoms in the growing cobalt oxide phase. This phenomenon has been described by the nanoscale Kirkendall effect and resulted in

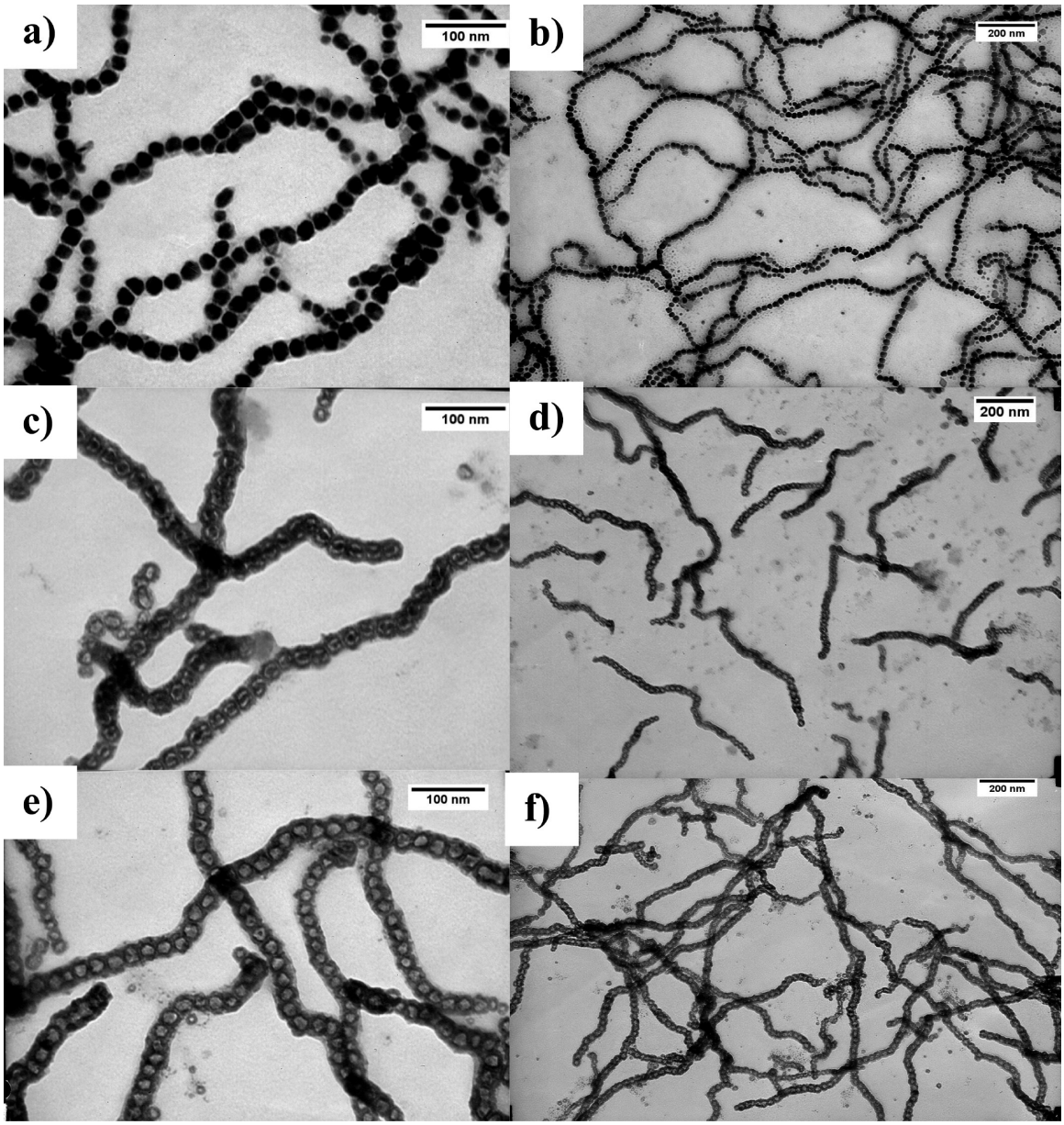

Figure 1. TEM images of the polystyrene-coated cobalt nanoparticles with particle size, $D = 20 \pm 2.4$ nm after oxidation for (a,b) 0 h; (c,d) 3 h, with particle diameter = 29 ± 2.7 nm, and (e,f) 1 week, with particle diameter = 32 ± 3.5 nm. All TEM samples were drop-casted from 0.5 mg/mL toluene dispersion onto a carbon-coated copper grid at zero field.

both the formation of hollow cores and a dimensional expansion of the cobalt oxide NP shell. PS-coated nanowires were formed because of the coalescence of expanding cobalt oxide NP shells formed in the oxidation reaction of preorganized PS-CoNP colloidal monomers. By varying the oxidation time of metallic PS-CoNPs in DCB, nonaggregated nanowires of either cobaltous oxide (PS-CoO), or cobalt cobaltite (PS-Co_3O_4) could be achieved as determined using X-ray diffraction (XRD) after a reaction time of 3 h or 1 week, respectively. The yields of these PS-coated cobalt oxide nanowires were also conducted on gram scales (yield = 1.04 g) that were enabled by improvements in the synthesis of ferromagnetic PS-CoNPs.

TEM and FE-SEM Imaging of PS-CoNPs and PS-Cobalt Oxide Nanowires. The formation of interconnected hollow nanowires was confirmed using transmission electron microscopy (TEM) of samples drop cast onto supporting surfaces (Figure 1a,b). The dipolar PS-CoNP precursors were imaged as discrete colloids ($D = 20$ nm $\pm$ 2.4 nm) assembled into NP-chains spanning micrometers in length. TEM showed that the native polymer-coated cobalt nanoparticles appeared as a dark solid sphere due to the high electron density of the cobalt core (Figure 1 a,b). After the oxidation reaction, a hollow inclusion in every cobalt oxide nanoparticle could be observed along the structurally intact 1-D nanostructure. The kinetics of the colloidal polymerization were followed by the removal of aliquots over varying reaction

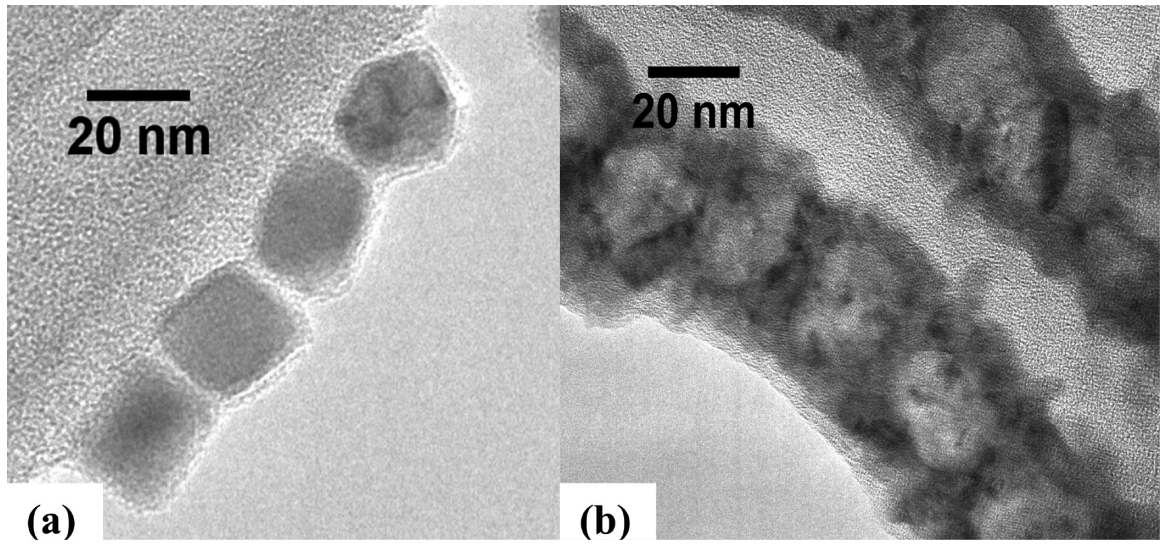

Figure 2. HRTEM of the (a) ferromagnetic PS-CoNP, (b) PS-Co_3O_4 nanowires after 1 week at 175 °C.

time for TEM imaging. After a reaction time of 3 h (Figure 1 c,d), three distinct regions of nanoparticle could be observed in TEM: (1) a lower electron density of the cobalt oxide shell, (2) a dark inner sphere of the cobalt core and (3) interior voids corresponding to the coalescence of vacancies at the interface. After 24 h, PS-coated cobalt oxide nanowires were observed to be completely hollow due to the conversion of metallic CoNPs into CoO phases, as indicated by XRD (see later discussion). As the oxidation time of PS-CoNPs in the DCB ferrofluid was extended over a period of 1 week, a similar morphology was observed. These hollow nanoparticles were also connected into a 1-D morphology (Figure 1 e,f) that spanned from several hundred nanometers to micrometers in length, as imaged *via* SEM (Figure 2).

High resolution TEM (HR-TEM) provided further evidence of 1-D connectivity of these cobalt oxide NPs into nanowires. HR-TEM imaging (Figure 2) confirmed that cobalt oxide NP shells were fused together to form 1-D chains after reaction times of 3 h (Figure 1), along with a dimensional expansion of nanowires from the conversion of PS-CoNPs into PS-CoO nanowires (D_{eff} = 29 nm). In contrast, PS-CoNPs precursors (D_{eff} = 20 nm) were imaged as discrete solid colloids that were separated by the outer PS shells (Figure 2a). An additional dimensional expansion of the cobalt oxide nanowire diameters (D_{eff} = 32 nm) were observed from HR-TEM over extended oxidation times of 1 week and were attributed to the gradual conversion of PS-CoO nanowires into Co_3O_4 phases (Figure 2b).

PS-CoNPs and PS-cobalt oxide nanowires were deposited onto ITO substrates *via* spin coating and imaged using field emission scanning electron microscopy (FE-SEM) to ascertain if discrete 1-D mesostructures were formed from the colloidal polymerization process. Thicker films of PS-cobalt oxide nanowires were cast onto ITO substrates and FE-SEM revealed the presence of nonaggregated 1-D chains that packed into a mesoporous film (Figure 3a). Discrete, nonagglomerated nanowires were also cast and imaged on ITO from dilute dispersions and were found to possess a distribution of chain lengths spanning hundreds of nanometers to several micrometers (Figure 3b), which was attributed to the step-growth-like nature of the colloidal polymerization of PS-CoNPs. FE-SEM qualitatively imaged morphology differences between the native PS-CoNPs and the PS-cobalt oxide nanostructures. SEM images of the PS-CoNPs (Figure 3c) showed 1-D chains of individual colloids that were associated *via* magnetostatic interactions, but separated by the polymer encapsulating shell. In contrast, PS-cobalt oxide nanowires were imaged *via* FE-SEM as beaded, but continuous 1-D mesostructures ranging from hundreds of nanometers to micrometers in length. (Figure 3d).

Solid-State Characterization of PS-Coated Cobalt Oxide and Calcined Co_3O_4 Nanowires. To further improve the crystallinity of the cobalt oxide phase within the nanowire and to remove the PS organic shell, the solution-deposited films on ITO were calcined at 400 °C in air for 16 h. Thermogravimetric analysis (TGA) of PS-coated nanowires confirmed that organics were fully degraded under these calcination conditions. FE-SEM of PS-Co_3O_4 films on ITO imaged the presence of 40 nm wide nanowires spanning micrometers in length. High resolution FE-SEM imaging visualized PS-coated nanowires possessing a relatively smooth surface morphology due to the glassy-like nature of the polymer shell (Figure 4a, b). FE-SEM after calcination revealed that the 1-D morphology of Co_3O_4 films were maintained, but the surface topography was considerably more roughened as evidenced by facets and small domains along oxidized nanowires (Figure 4c,d). We have also confirmed *via* TEM that both the 1-D morphology and the porous inclusions of Co_3O_4 nanowires were preserved after the calcination process (see Supporting Information, Figure S-1).

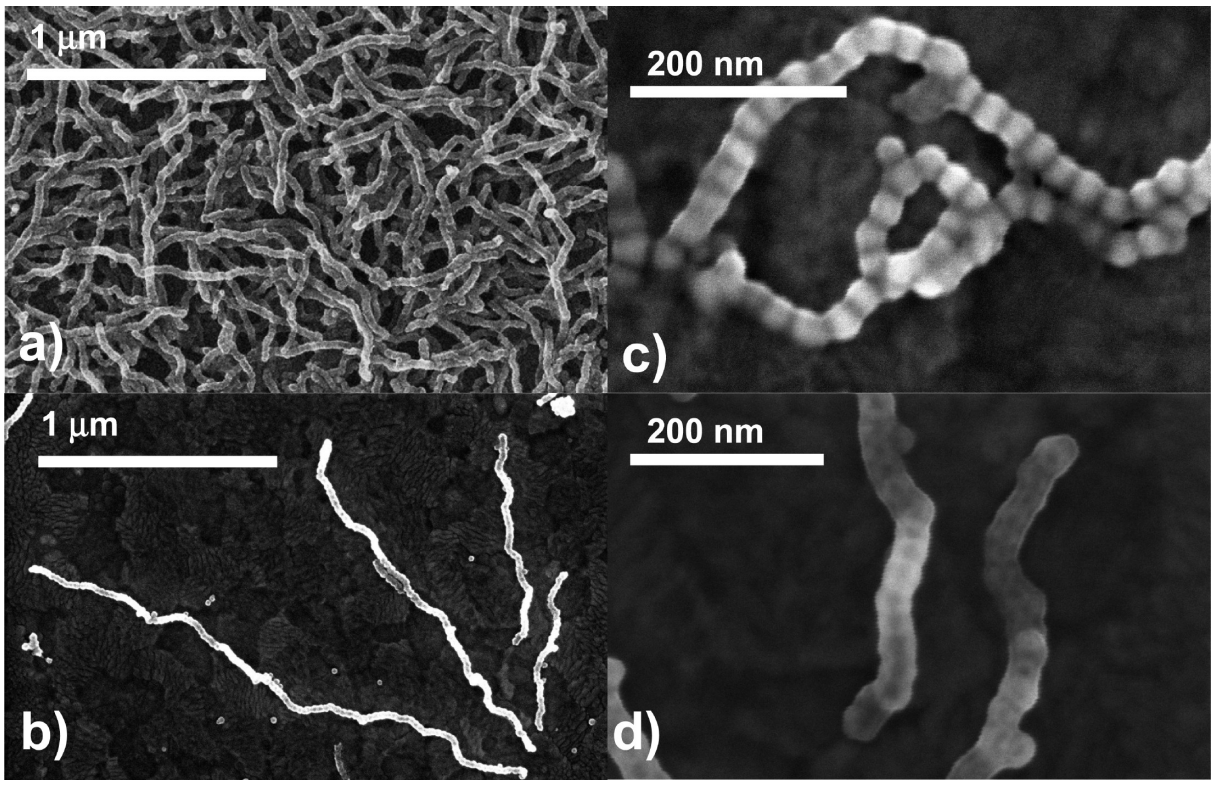

Figure 3. FE-SEM images of thick films (a) and isolated nanowires (b) of PS-Co_3O_4 materials spin coated onto ITO; (c) high magnification FE-SEM of discrete chains of PS-CoNPs; (d) high magnification FE-SEM of PS-Co_3O_4 single nanowires.

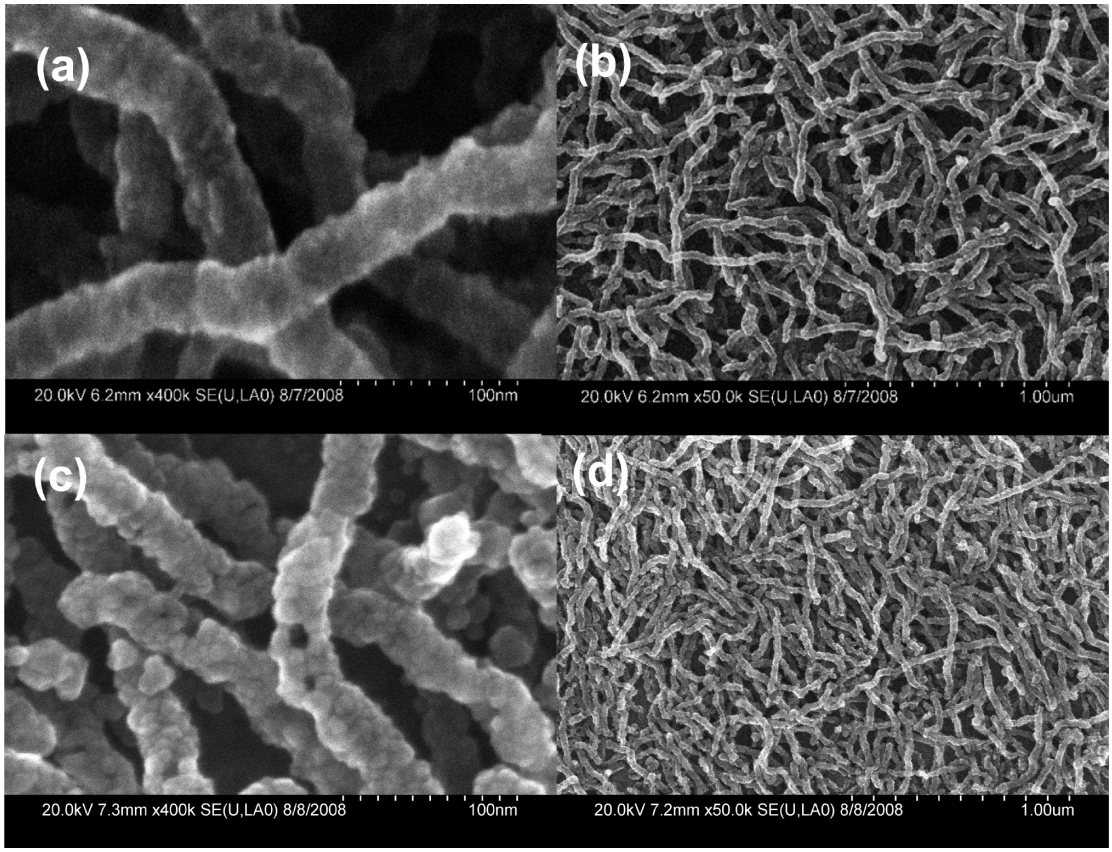

Figure 4. FE-SEM images of PS-Co_3O_4 nanowires cast on ITO at both high (a) and low (b) magnification and after calcinations in air at 400 °C at high (c) and low (d) magnification.

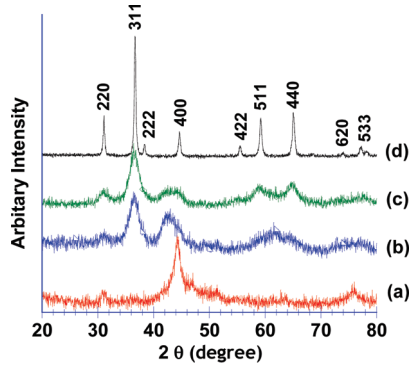

Figure 5. Overlay XRD patterns of the (a) polystyrene-coated cobalt nanoparticles, (b) polystyrene-coated cobalt oxide after 3 h of oxidation, (c) after 1 week of oxidations, and (d) after calcination at 400 °C in air. The diffraction peaks were indexed to the spinel-Co_3O_4 phase.

Powder X-ray diffraction was used to characterize the solid-state structure of PS-CoNP, PS-coated nanowires and calcined cobalt oxide materials. The XRD results confirmed the initial PS-CoNP precursors exhibited a metallic fcc-cobalt phase of low crystallinity (Figure 5a) Subsequent oxidation of PS-CoNPs in DCB at 175 °C over a 3 h period converted these precursors to a mixture of rock salt-CoO and residual fcc-cobalt (Figure 5b). Prolonged oxidations of PS-CoNPs over a period of 1 week predominantly yielded an amorphous phase of Co_3O_4 (Figure 5c). Further calcination of PS-CoO NPs in air at 400 °C burned out the organic PS outer shells and yielded polycrystalline spinel Co_3O_4 material, in which all diffraction peaks were indexed to bulk spinel Co_3O_4 (Figure 5d).

The magnetic properties of PS-coated and calcined cobalt oxide nanocomposites were measured using vibrating sample magnetometry (VSM) at room temperature and at 60 K (Figure 6). The general trend from the magnetometry indicated that both the saturation magnetization ($\mathbf{M}_s$) and coercivity ($\mathbf{H}_c$) significantly decreased after the colloidal polymerization process which was in agreement with the formation of antiferromagnetic CoO and Co_3O_4. The native PS-CoNPs (Figure 6a,1), exhibited weakly ferromagnetic behavior at room temperature ($\mathbf{M}_s$ = 41.2 emu/g; $\mathbf{H}_c$ = 713 Oe). The magnetometry at room temperature revealed that PS-CoO materials (Figure 6a,2) were weakly ferromagnetic after a 3 h oxidation in DCB and exhibited a significant decrease in the saturation magnetization ($\mathbf{M}_s$ = 4.6

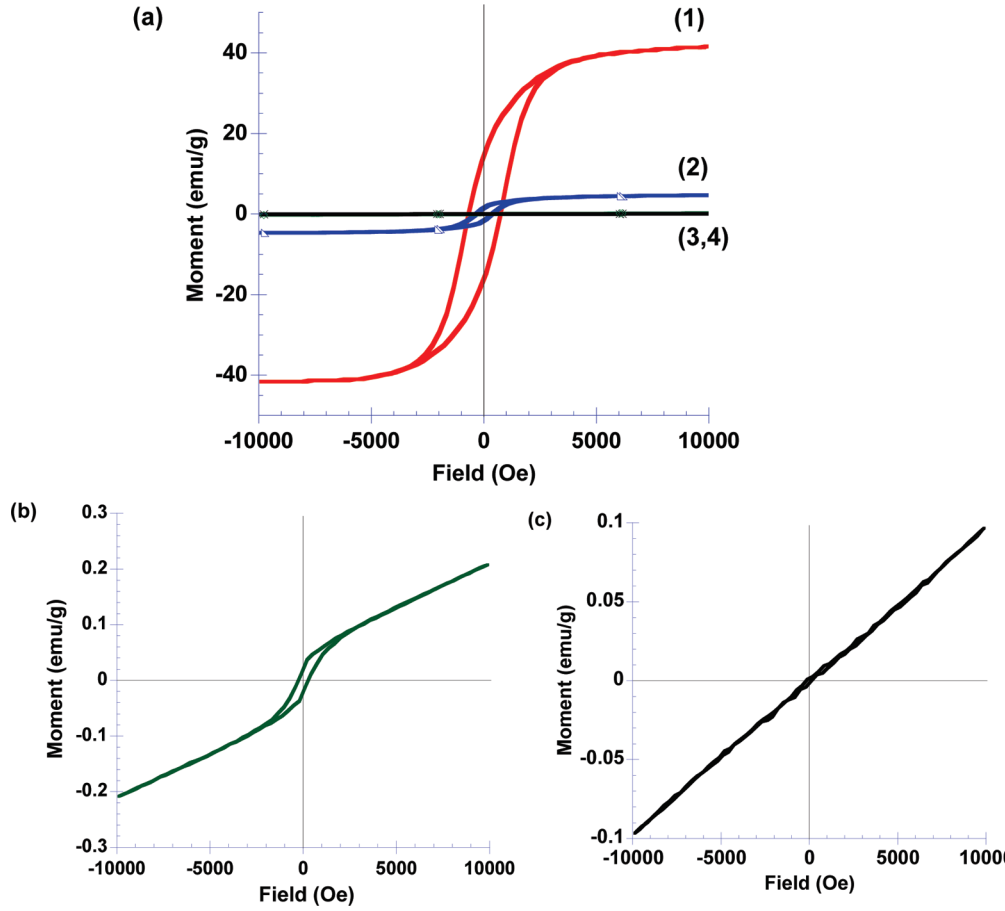

Figure 6. (a) Overlay hysteresis curves of applied magnetic field (H) *vs* magnetization ($\mathbf{M}_s$) of nanocomposites 1−4 at 27 °C: PS coated CoNPs (1), polystyrene-coated cobalt oxide after 3 h of oxidation (2), polystyrene-coated cobalt oxide after 1 week of oxidation (3), and bare Co_3O_4 nanowires after calcination at 400 °C (4); (b) high resolution magnetometry of of PS-coated cobalt oxide materials after 1 week oxidation time (3); (c) high resolution magnetometry of calcined Co_3O_4 nanowires after calcination in air at 400 °C.

emu/g) and coercivity ($\mathbf{H}_c$ = 362 Oe) at room temperature. This ferromagnetic behavior was attributed to the presence of residual metallic cobalt, which was further supported by the XRD data in Figure 5. Similar magnetization behavior was also observed in wurtzite CoO, in which the presence of metallic Co impurities resulted in a hysteresis curve.[90] The magnetization ($\mathbf{M}$ = 2.07 emu/g at 10000 Oe) and coercivity ($\mathbf{H}_c$ = 260 Oe) of PS-Co_3O_4 were further decreased by prolonged 1 week oxidation times. The magnetometry of PS-Co_3O_4 materials exhibited a linear relationship of magnetization ($\mathbf{M}$) *vs* applied field ($\mathbf{H}$) behavior due to the presence of rock-salt CoO and spinel Co_3O_4 phases as indicated by the linearity of magnetometry above and below 5000 and −5000 Oe (Figure 6b). The magnetometry of the PS-coated Co_3O_4 nanocomposite (Figure 6b) also exhibited weakly ferromagnetic behavior as evidenced by a small hysteresis which was attributed to trace Co metal. Calcined Co_3O_4 nanowires (Figure 6c) exhibited a linear magnetization curve with a reduced $\mathbf{M}$ value. The linear curve was consistent with the paramagnetic behavior of Co_3O_4 nanoparticles at room temperature as reported elsewhere.[91]

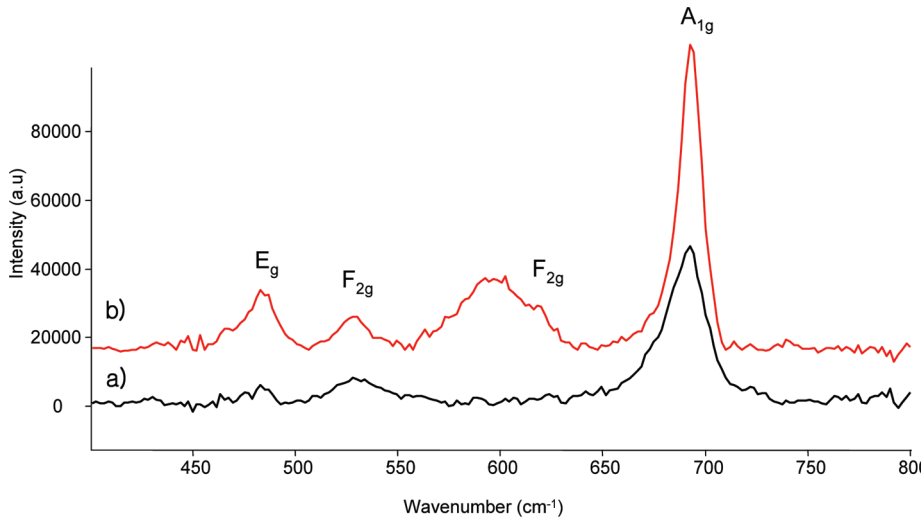

Figure 7. Raman spectroscopy of films on Ag substrates of (a) PS-Co_3O_4 nanowire films after solution oxidation times in DCB at 170 °C for 1 week, and (b) calcined Co_3O_4 nanowires after thermal treatment in air at 400 °C.

Spectroscopic Characterization of Co_3O_4 Nanowires. Characterization of polymer-coated and calcined cobalt oxide nanowires was conducted using Raman spectroscopy to confirm the formation of the spinel Co_3O_4 phase (Figure 7). Raman spectroscopic characterization was complicated by the strong absorption of Co_3O_4 films in the visible wavelength regime, as evidenced by the black appearance of this material. Although Raman spectroscopic characterization of Co_3O_4 materials has primarily been conducted using microprobe Raman techniques, we were able to acquire quality Raman spectra of Co_3O_4 nanowire films using standard approaches by processing of thin films on reflective Ag substrates. PS-coated cobalt oxide nanowires were spin-coated onto clean Ag subtrates and measured both before and after calcination reactions in air at 400 °C. The preparation of PS-Co_3O_4 nanowires after a solution oxidation time of 1-wk was confirmed in the Raman spectra by the presence of peaks at 483, 528, and 692 cm^{-1}, which correspond to E_g, F_{2g}, and A_{1g} vibrational modes, respectively, for Co_3O_4.[18,46,92] After calcination of PS-coated nanowires, sharper and more intense peaks at 483, 528, and 692 cm^{-1} were observed. In addition, the A_{1g} peak shifted from 690 to 692 cm^{-1}, which has been correlated with an enhancement in electrical conductivity of Co_3O_4 thin films.[92] After calcination, an additional broad peak at 600 cm^{-1} was observed and assigned to a second F_{2g} mode that was expected based on previous Raman assignments of Co_3O_4 thin films. However, the relative intensity of this peak at 600 cm^{-1} was intuitively too high to arise solely from the formation of more crystalline Co_3O_4 nanowire thin films and was identified to be trace graphitic carbon (other broad carbon peaks around 1600 and 1350 cm^{-1} also observed) that was formed from pyrolysis of the organic PS coating.

X-ray photoelectron spectroscopy (XPS) was also used to confirm the formation of Co_3O_4 nanowires after calcination in air at 400 °C. Al Kα XPS was conducted of thin films deposited onto ITO substrates and measured in the regions of Co_{2p} and O_{1s} binding energy regions. XPS in the Co_{2p} region of binding energies exhibited two major peaks at 796.1 and 780.6 eV that corresponded to $2p_{1/2}$ and $2p_{3/2}$ spin−orbit components, respectively, with the $Co_{p1/2}$ peak at 796.1 eV being more intense (Figure 8). Weaker satellite peaks at

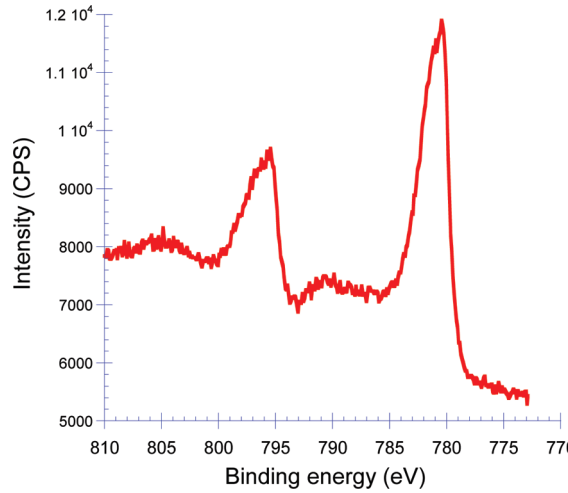

Figure 8. Co_{2p} XPS spectroscopy of calcined Co_3O_4 nanowires after thermal treatment in air at 400 °C.

790.5 and 805.5 eV were also observed in the Al−Ka XPS. The formation of these peaks has been extensively observed in thin films of cobalt oxides prepared from a variety of methods and were attributed to surface hydroxide species from exposure to air.[18,46,93−95]

Spectroscopic Determination of Band Edge Energy Levels of Co_3O_4 Nanowires. Optical absorption spectroscopy and ultraviolent photoelectron spectroscopy (UPS) were conducted to determine the band edge energy levels of Co_3O_4 nanowires calcined at 400 °C. UV−visible absorption spectroscopy of Co_3O_4 nanowire films on ITO revealed two broad absorption bands centered around 450 and 750 nm, which were consistent with other literature reports on the optical properties for spinel type Co_3O_4 thin films.[46,47,94−96] The optical band gap energies were determined using the Tauc plot method and were in reasonable agreement with previous spectroscopic studies of cobalt oxide thin films indicative of two optical transitions at 1.45 and 2.26 eV.[46,47,94−98]

The optical transition from Co_3O_4 nanowires at 2.26 eV was attributed to a band gap transition from the valence band of the metal oxide, which was proposed to comprise a mixture of both $Co^{2+,3+}$ 3d and O 2p states. The lower energy transition at 1.45 eV was assigned to transitions from midgap states[99] into the conduction band due to the presence of defect sites within these hollow Co_3O_4 nanowires. As previously discussed, Co_3O_4 nanowires prepared *via* colloidal polymerization resulted in the formation of hollow inclusions in nanoparticle repeating units that were fused along the 1-D mesostructure. As a result, these nanomaterials were anticipated to contain defect sites in the metal oxide phase, as a likely consequence of a greater number of surface Co ion sites accompanied by ion vacancies in the partially coordinated $Co^{2+,3+}$ ions within the spinel Co_3O_4 lattice.[93,99] These assumptions were based on the presence of both hollow interior inclusions along the nanowire and the high degree of corrugation on the surface of calcined Co_3O_4 materials as observed *via* TEM (Figure 2b) and FE-SEM (Figure 4c), respectively. These band gap and midgap states assignments were also supported by modeling and valence band photoemission studies of nonstoichiometric Co_3O_4 films, in which the valence band was assigned to a mixture of both $Co^{2+,3+}$ 3d and the O 2p states.[93,97] Extensive reports on the optical spectroscopy of Co_3O_4 materials have assigned these optical transitions to two direct band gaps from solely O 2p states in the valence band into Co^{2+} 3d conduction band states at 2.26 eV and into Co^{3+} conduction band 3d states at 1.45 eV.[46,47,94−96] However, given the strong likelihood of defect sites being present in Co_3O_4 nanowires prepared *via* colloidal polymerization, it is anticipated that optical transitions observed were not from two direct band gaps but arose from discrete band gap and midgap transitions.

Because of the novel nanoscale structure of the cobalt oxide nanowires prepared *via* colloidal polymerization, UPS of calcined Co_3O_4 nanowire on Au substrates was conducted to determine the highest energy of the valence band (VB) in the metal oxide semiconductor. In the UPS experiment, the kinetic energy of the photoexcited electrons emitted from Co_3O_4 films were measured assuming electrical equilibration between the Au substrate, in which a common Fermi level ($E_f = 0$) was established (Figure 10). Because electrical contact and equilibrium between the Au substrate and the thin film was required, UPS measurements of PS-coated nanowires were not conducted. While more detailed UPS studies have been conducted with full spectroscopic assignments of photoemitted electrons from Co_3O_4 thin films,[93] our interest for this investigation was focused on the determination of highest energy levels of the Co_3O_4 VB. The UPS spectrum of Co_3O_4 on a Au substrate shown in Figure 10a has been normalized to the Fermi level of Au, in which $E_f = 0$. The edge of the highest energy population of the VB for Co_3O_4 was observed as a sharp increase at −0.5 eV relative to the mutual Fermi level of Au and the spectrometer ($E_f = 0$) in the UPS spectrum, while the lowest energy electrons were found at the −16.4 eV. The absolute difference in energies between the lowest and highest kinetic energy edges of the UPS spectrum was defined as the spectral width (SW), which afforded a SW = 15.9 eV. The threshold ionization potential (IP) of the Co_3O_4 nanowire material was obtained as the difference of the incident photon energy (for He(I) source = 21.2 eV) and the spectral width (15.9 eV) of the UPS spectrum (Figure 10a),[100] which afforded an IP = 5.3 eV.

From the UPS IP data, the energy of the Co_3O_4 VB with respect to vacuum was set to 5.3 eV, which in conjunction with the optical band gaps determined from the optical absorption spectroscopy (Figure 9), afforded a proposed band edge energy diagram for calcined Co_3O_4 nanowires as shown in Figure 10c. Because of the polycrystalline nature of the Co_3O_4 nanowires prepared *via* colloidal polymerization, an assignment of the exact valence band and conduction band was difficult, because earlier calculations and modeling of band edge energies was primarily based on crystalline Co_3O_4.[93,99] On the basis of the thorough photoemission studies on Co_3O_4 epitaxy film by Langell[93] and the optical band gap measurements (Figure 9), the highest energy level of valence band was assigned to a mixture of $Co^{2+,+3}$ ions *3*d and O 2p orbitals with a band gap energy of 2.26 eV and a midgap transition of 1.45 eV. It is important to note that the values of the Co_3O_4 VB (5.3 eV) and conduction bands (3.04 eV) are determined from UPS in vacuum and may deviate from values determined photoelectrochemically *via* Mott−Schottky measurements since solvent effects were not accounted for using the described methodology.

The current density (*J*)−voltage (*V*) characteristics of calcined Co_3O_4 nanowires were determined *via* conductive probe atomic force microscopy (C-AFM). Nanowires

were spin-coated onto Pt-coated Si subtrates and then analyzed with a Pt tip for C-AFM $J-V$ measurements in 20 μm^2 areas, with a bias of $+1.0$ to -1.0 V in air at room temperature. The wormlike morphology of the Co_3O_4 nanowires (Figure 11a) was first resolved by tapping mode AFM using a silicon nitride cantilever. In height contrast imaging, bright features were assigned to the Co_3O_4 nanowires, while dark regions corresponded to voids formed from the interdigitation of 1-D components, which was consistent with the FE-SEM of the calcined film (Figure 3a). The topography of the film was also imaged in tapping mode using a Pt cantilever for C-AFM prior to electrical probing as shown in Figure 11b; however, resolution of nanowire features was compromised because of the use of nonoptimal Pt tips for visualization of individual nanoscale wires. Nevertheless, these Pt tips were effective in current contrast C-AFM, which imaged very delicate nanoscale features, confirming that nanowires were uniformly conductive, as visualized as bright regions corresponding to Co_3O_4 semiconducting nanowires (Figure 11c). Darker features in current-mapped C-AFM images also corresponded to porosity generated from the void spaces in the nanowire thin film. The $J-V$ characteristics of these Co_3O_4 NP films revealed a linear relationship (Figure 11e) from -0.12 to $+0.12$ V, indicative of Ohmic contact between the Pt tip and Co_3O_4 nanowires, while space-charge limiting current was observed above these potentials.[101] The symmetrical $J-V$ plot further showed that these Co_3O_4 nanowires were in Ohmic contact with both the Pt tip junction as well as the Pt substrate on the bottom contact. This current-voltage behavior was consistent with the predicted behavior of Co_3O_4, which is a p-type semiconductor with electrical conductivity arising from hole carriers.[92] Quantitative determination of carrier mobilities *via* C-AFM was complicated by the 1-D nanoscale morphology of Co_3O_4 nanowires due to the additional geometrical terms in the space charge-limited current equation that is only valid for solid films. Quantitative measurements of electrical conductivity are currently in progress *via* microwave techniques.

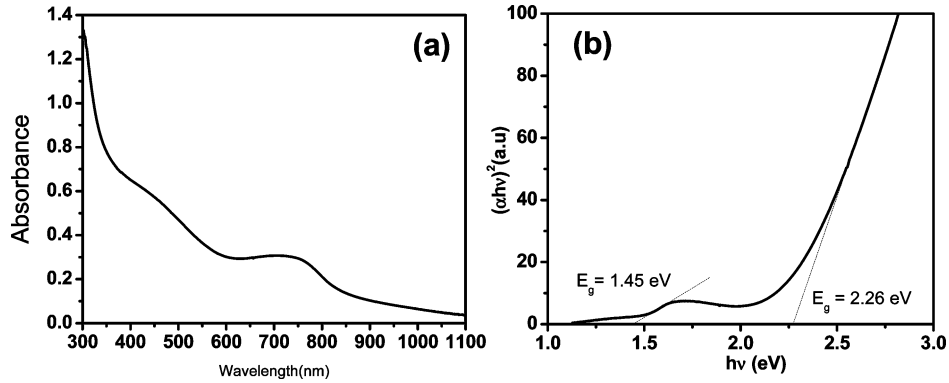

Figure 9. (a) UV−vis spectra of calcined Co_3O_4 nanowires on ITO. (b) Optical band gap energy Co_3O_4 nanowires obtained by extrapolation to $\alpha = 0$.

Cyclic Voltammetry (CV) of Calcined Co_3O_4 Nanowire Films on ITO. Cyclic voltammetry was used to characterize calcined Co_3O_4 nanowire films on ITO. To afford polycrystalline Co_3O_4 materials, PS-Co_3O_4 films on ITO were first calcined in air at $T = 400$ °C prior to electrochemical measurements and cleaned by exposure to UV−ozone to remove residual organics from the metal oxide surfaces. FE-SEM of calcined films confirmed that the 1-D morphology of nanowires remained intact, as discussed previously (see

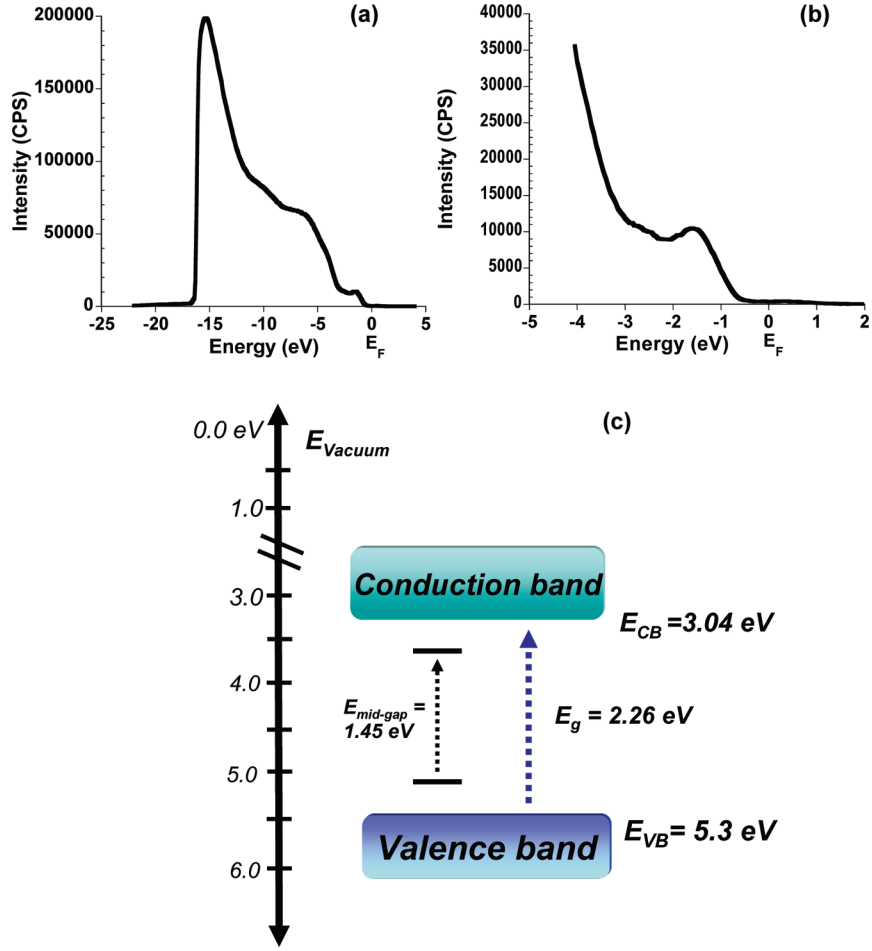

Figure 10. Low (a) and high resolution (b) UPS spectra of calcined Co_3O_4 nanowires after thermal treatment in air at 400 °C on Au substrates, and (c) energy level diagram for band edge energies for calcined Co_3O_4 nanowires.

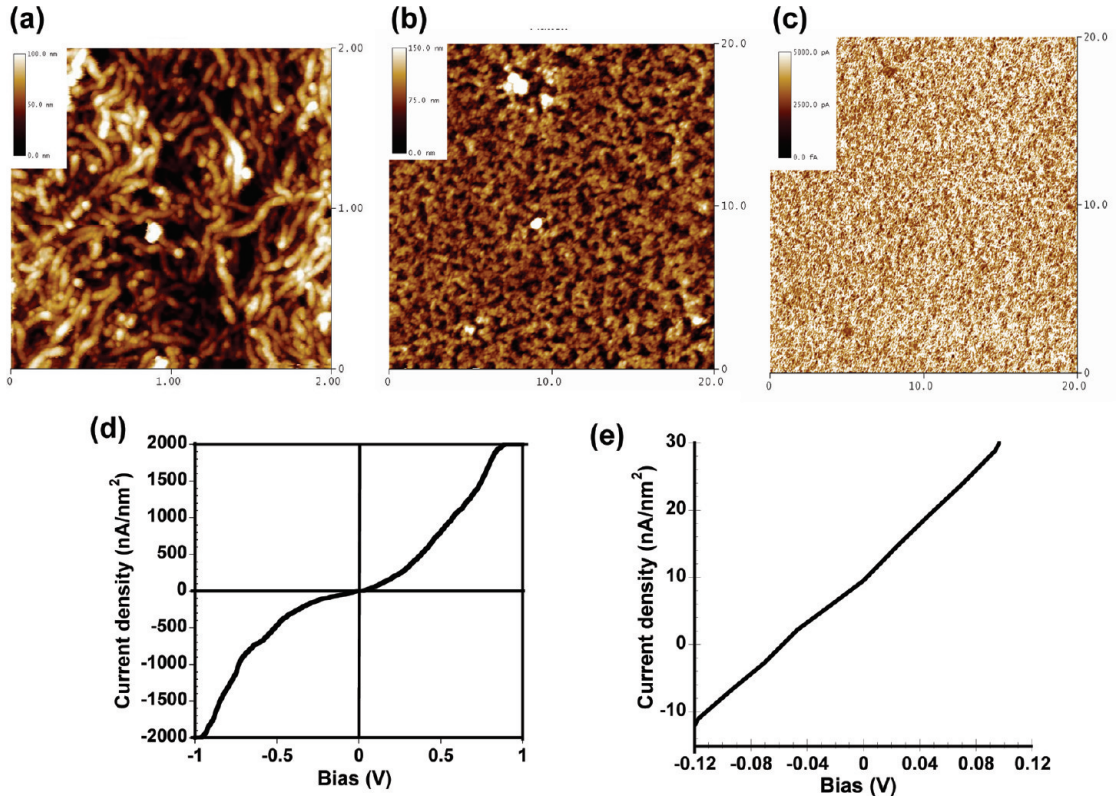

Figure 11. Tapping mode and conductive probe AFM images of calcined Co_3O_4 nanowires with (a) height contrast image (2 μm × 2 μm) in tapping mode using a silicon nitride cantilever, (b) height contrast image (20 μm × 20 μm) in tapping mode using a conductive Pt cantilever, (c) current contrast imaging (20 μm × 20 μm) using a Pt cantilever from +1.0 to −1.0 V, and (d) current density *vs* voltage plot of calcined Co_3O_4 nanowires (e) linear relationship in the current density *vs* voltage plot of calcined nanowires from −0.12 to +0.12 V showing an Ohmic behavior at the Pt/Co_3O_4 junction.

Figure S1 for TEM, Figure 4 for SEM, and Figure 6d for XRD). Cyclic voltammetry was performed on the films in 0.1 M NaOH electrolyte solution while cycling from 0.7 to −0.9 V at 20 mV/s with respect to a Ag/AgCl (3 M KCl) reference electrode (Figure 12). Multiple peaks within the voltammogram were consistent with the formation of a number of cobalt oxide phases at different oxidation states, specifically, anodic peaks at 0, 0.2, and 0.6 V and corresponding cathodic peaks at 0.5, 0.2, and −0.5 V. Assignments of these peaks were in agreement with previously reported phases of cobalt in water in the Pourbaix diagram and other recent reports which can be associated with the following reactions:[10,21,22,102−104]

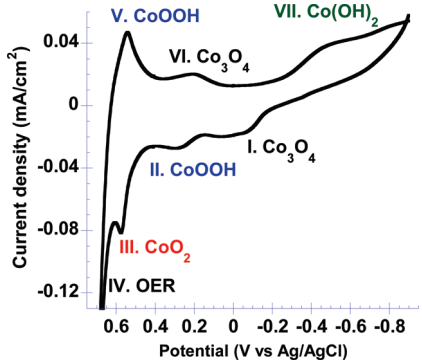

Figure 12. CV of calcined Co_3O_4 film on ITO at 20 mV/s scan rate in 0.1 M NaOH electrolyte solution.

Anodic Scan (toward Positive Potentials).

peak I (0.3 V), Co_3O_4 formation:

$$3Co(OH)_2 + 2OH^- \rightleftharpoons Co_3O_4 + 4H_2O + e^- \quad (1)$$

peak II (0.5 V), CoOOH formation:

$$Co_3O_4 + OH^- + H_2O \rightleftharpoons 3CoOOH + e^- \quad (2)$$

peak III, CoO_2 formation:

$$CoOOH + OH^- \rightleftharpoons CoO_2 + H_2O + e^- \quad (3)$$

peak IV, oxygen evolution reaction (OER):

$$4^-OH \rightleftharpoons O_2 + 2H_2O + 4e^- \quad (4)$$

Cathodic Scan (toward Negative Potentials).

peak V, CoOOH formation:

$$CoO_2 + H_2O + e^- \rightleftharpoons CoOOH + OH^- \quad (5)$$

peak VI, Co_3O_4 formation:

$$3CoOOH + e^- \rightleftharpoons Co_3O_4 + OH^- + H_2O \quad (6)$$

peak VII, $Co(OH)_2$ formation:

$$Co_3O_4 + H_2O + 2e^- \rightleftharpoons 3(Co(OH)_2 + 2OH^- \quad (7)$$

As previously determined by powder XRD (Figure 6d), the initial state of the calcined cobalt oxide nanowires was found to be polycrystalline Co_3O_4 phase, which consisted of both the Co^{2+} and Co^{3+} oxidation

states and can be seen in the cyclic voltammogram (peak I). In the anodic scan, from potential 0 to 0.2 V, the Co_3O_4 phase was oxidized to the cobalt oxyhydroxide (CoOOH) phase with a Co^{3+} oxidation state and an uptake of hydroxide ions and water from the electrolyte media (peak II-eq 2). Further anodic scanning to 0.6 V resulted in oxidation of the CoOOH to cobalt peroxide (CoO_2) with a Co^{4+} oxidation state and condensation reactions to release water (peak III, eq 3). A large anodic peak in the voltammogram at 0.7 V was observed and attributed to electrocatalytic oxygen evolution (OER) by the Co_3O_4 nanowire thin film (peak IV, eq) accompanied by the formation of bubbles in the electrochemical cell. In the cathodic scan to 0.5 V resulted in the reduction of CoO_2 to CoOOH, followed by the reduction to Co_3O_4 at 0.2 V. Further cathodic scan to −0.5 V resulted in the reduction of Co_3O_4 to $Co(OH)_2$ (peak VII, eq 6). As shown in Figure 10, these nanostructured cobalt oxides prepared *via* colloidal polymerization (*i.e.*, magnetic assembly and nanoscale Kirkendall reaction) undergo electrochemical charge transfer reactions Co(II) ↔ Co(III)) ↔ Co(IV) in basic electrolyte, making these nanowires potential candidates for pseudocapacitive electrodes in hybrid electrochemical capacitors.[2]

CONCLUSION

Colloidal polymerization of ferromagnetic PS-CoNPs into 1-D cobalt oxide nanowires is reported. We demonstrate that the combination of dipolar assembly and oxidation of dipolar nanoparticles is a facile and robust method to prepare well-defined polymer-coated cobalt oxide nanowires in gram scale quantities. We also demonstrate for the first time that these nanostructured cobalt oxide materials are electrically and electrochemically active and of interest for potential applications in energy storage. Future work will examine the effect of the nanoporosity of these cobalt oxide wires as electrochemical supercapacitors and investigate Li ion insertion for Li batteries.

EXPERIMENTAL SECTION

Materials and Characterization. Anhydrous 1,2-dichlorobenzene (DCB), toluene (99.5%), lithium perchlorate ($LiClO_4$, 95%), and NaOH (99.99%) were purchased from Aldrich and used as received without further purification. Dicobalt octacarbonyl ($Co_2(CO)_8$) was purchased from Strem Chemicals and used as received. Compressed oxygen gas was purchased from Matheson Trigas. Thermolysis reactions were performed using an Omega temperature controller CSC32 with a K-type utility thermocouple and a Glas-Col fabric heating mantle. Calcination of the polymer-coated cobalt oxide nanowires was performed in a Barnstead/Thermolyne small benchtop muffled furnace at 400 °C in air. Indium-doped tin oxides-coated glass (ITO) was obtained from Colorado Concept Coatings, LLC. Electrochemical measurements were performed with a CH-instrument 600c potentiostat/galvanostat in a home-built Teflon compression cell (electrode area ~0.7 cm^2) sealed with perfluoroelastomer O-rings (Kalrez). A Pt coil and Ag/AgCl electrode (sat. KCl) were used as the counter and reference, respectively. The reference electrode was calibrated using a saturated calomel electrode (~44 mV *vs* SCE). UV−vis spectra were obtained using an Agilent UV−vis spectrometer (no. 8453A, Foster City, CA). TEM images were obtained on a JEM100CX II transmission electron microscope (JEOL) at an operating voltage of 60 kV, using in-house prepared carbon-coated copper grids (Cu, hexagon, 400 mesh) and carbon-coated nickel grids (Ni, hexagon, 300 mesh). Image analysis was performed using ImageJ software (Rasband, W.S., National Institute of Health, http://rsb.info.nih.gov/ij/, 1997−2007). Relative uncertainty of particle size determinations using ImageJ was found to be 1% of diameter average (*e.g.*, 20 ± 0.2 nm). SEM images were taken on a Hitachi 4800 FE-SEM (20 kV accelerating voltage) on the as-prepared sample (*i.e.*, no metallic overcoating). AFM measurements were performed on a Digital Instrument Dimension 3100 scanning probe microscope in tapping mode. Conducting-tip AFM (C-AFM) measurements were made with a Dimension 3100 Nanoscope IV system (Veeco Metrology Group, Santa Barbara, CA) with the TUNA application module. Conducting Pt-coated CSC38/Pt tips were procured from Mikromasch with a nominal force constant of 0.08 N/m. C-AFM measurements were made in contact mode in air with minimal force engagement, followed by a well-calibrated and controlled force load (3 N/m) at the conductive probe. The samples of investigation were made on a platinum-coated silicon wafer which was held through the vacuum chuck that provided sample bias with respect to the conductive probe that was kept at ground potential. Both height and TUNA current channels were displayed and recorded upon application of an appropriate amount of sample bias. Current sensitivity was chosen on the basis of the nature of the sample which was 10 nA/V in the present case. VSM measurements were obtained using a Waker HF 9H electromagnet with a Lakeshore 7300 controller and a Lakeshore 668 power supply. Magnetic measurements were carried out at room temperature (27 °C or 300 K) and low temperature (−213 °C or 60 K), with a maximum S-2 applied field of 1190 kA/m, a ramp rate of 2630 A m^{-1} s^{-1} and a time constant of 0.1. XRD measurements were performed using the X'pert X-ray diffractometer (PW1827) (Phillips) at room temperature with a Cu Kα radiation source at 40 kV and 30 mA. UPS and XPS analyses were conducted in a combined UPS-XPS Kratos Axis Ultra 165 with an average base pressure of 10^{-9} Torr. XPS data were collected with monochromatic Al Kα radiation at a pass energy of 20 eV. UPS spectra were obtained with a 21.2 eV He (I) excitation (SPECS UVS 10−35) and pass energy of 5 eV. For all UPS analyses, a 9 V bias was applied to improve the transmission of low KE electrons and to improve the determination of the energy of the low-KE edge. Separate UPS spectra and XPS spectra were measured frequently for an atomically clean gold sample to calibrate the Fermi energy (E_F). XPS spectra were acquired before UPS data acquisition. All characterization experiments were performed at normal takeoff angle (0°) unless otherwise noted. Raman spectra were acquired with 5 mW of radiation at 514.5 nm from a Coherent Innova 350C Ar^+ laser. Plasma lines were removed using a bandpass filter (3.0 nm bandwidth) from Pomfret Research Optics. Scattered light was collected and collimated by a plano-convex lens and passed through a holographic SuperNotch Plus filter (Kaiser Optical Systems) before being focused through a polarization scrambler and a second SuperNotch Plus filter onto the 50 μm entrance slit of a Spex 270 M monochromator. This monochromator utilizes a 1200 gr/mm grating blazed at 630 nm resulting in a spectral bandpass of 1 cm^{-1}. A 1340 × 400 pixel, thinned, back-illuminated CCD (Roper Scientific model 400-EB) held at −95 °C was used for detection. Images from this detector were processed by WinSpec32 software (Roper Scientific) and then were imported into Grams 32 (Galactic Industries) for spectral calibration and manipulation. Spectra were calibrated using known Ar^+ emission lines observed by removing the laser bandpass filter. Typical integration times varied from 120−180 min per acquisition, accomplished by coaddition of individual 6 s integrated spectra.

Preparation of Amine End-Functional Polystyrene Surfactants (PS-NH_2). PS-NH_2 was synthesized according to our previous report.[105]

Preparation of PS-CoNPs (1), Using Amine End-Functional Polystyrene Surfactants, PS-NH_2. PS-NH_2 (0.400 g; 7.27×10^{-2} mmol) was dissolved in DCB (10 mL) and transferred into a three- neck round-bottom flask containing DCB (30 mL) and heated to 175 °C. Separately, $Co_2(CO)_8$ (1.00 g; 2.92×10^{-3} mol) was dissolved in DCB (8 mL) at room temperature in air, and was rapidly injected into the hot polymer solution *via* syringe. Upon injection, the reaction temperature dropped to 160 °C and the reaction mixture was maintained at 160 °C for 60 min followed by cooling to room temperature under argon. PS-CoNPs were isolated by precipitation into hexanes (500 mL), yielding a black powder (yield = 0.784 g) that was soluble in a wide range of organic solvents (*e.g.*, methylene chloride, THF, toluene). The sample for TEM analysis was prepared by dispersing the isolated powder (1 mg) in toluene (2 mL) *via* sonication for 15 min followed by drop casting onto a carbon-coated Cu grid. The particle size of the PS-CoNPs was determined to be 20 ± 2.4 nm *via* TEM. Magnetic properties of PS-CoNPs were measured using VSM at room temperature: $\mathbf{M}_s$ = 41.2 emu/g, $\mathbf{H}_c$ = 713 Oe; and at 60 K, $\mathbf{M}_s$ = 43.7 emu/g, $\mathbf{H}_c$ = 1440 Oe. TGA analysis showed 41% of organics by mass.

Preparation of PS-Co0 Nanostructures (2). A three-neck round-bottom flask equipped with a reflux condenser and a stir bar was charged with 16 mL of the as-prepared ferrofluid of PS-CoNPs. The ferrofluid was heated to 175 °C and stirred at 300 rpm, while bubbling with oxygen for 3 h of oxidation. The mixture was then allowed to cool to room temperature. The ferrofluid was isolated by precipitation into hexanes (500 mL), followed by centrifugation at 5000 rpm for 15 min to yield a black powder (yield = 0.302 g) that was soluble in a wide range of organic solvents (*e.g.*, methylene chloride, THF, toluene). TEM sample was prepared as previously described. The diameter of the PS-cobalt oxide nanowire **2** was determined to be 29 ± 2.7 nm *via* TEM. Magnetic properties of PS-cobalt oxide **2** were measured using VSM at room temperature: $\mathbf{M}_s$ = 4.6 emu/g, $\mathbf{H}_c$ = 363 Oe; and at 60 K, $\mathbf{M}_s$ = 4.8 emu/g, $\mathbf{H}_c$ = 734 Oe. TGA analysis showed 34% of organics by mass.

Preparation of PS-Co_3O_4 Nanostructures (3). A three-neck round-bottom flask equipped with a reflux condenser and a stir bar was charged with 48 mL of the as prepared ferrofluid (c = 16 mg/mL). The ferrofluid was heated to 175 °C and stirred at 300 rpm, while bubbling with oxygen for 1 week of oxidation. It was then allowed to cool to room temperature. The ferrofluid was isolated by precipitation into hexanes (500 mL) followed by centrifugation at 5000 rpm for 15 min to yield a black powder (yield = 0.575 g) that was soluble in a wide range of organic solvents (*e.g.*, methylene chloride, THF, toluene). The TEM sample was prepared as previously described. The diameter of the PS-cobalt oxide nanowire **3** was determined to be 32 ± 3.5 nm *via* TEM. Magnetic properties of PS-cobalt oxide **3** were measured using VSM at room temperature: **M** = 0.2 emu/g at 10000 Oe; and at 60 K, **M** = 0.38 emu/g at 10000 Oe. TGA analysis showed 11% of organics by mass.

Preparation of PS-CoNPs, Using Amine End-Functional Polystyrene Surfactants, PS-NH_2 on Gram Scale. PS-NH_2 (1.30 g; 2.89×10^{-1} mmol) was dissolved in DCB (10 mL) and transferred into a three-neck round-bottom flask containing DCB (30 mL) and heated to 175 °C. Separately, $Co_2(CO)_8$ (2.00 g; 5.85×10^{-3} mol) was dissolved in DCB (12 mL) at room temperature in air, and was rapidly injected into the hot polymer solution. Upon injection, the reaction temperature dropped to 160 °C and the reaction mixture was maintained at 160 °C for 60 min followed by cooling to room temperature under argon. PS-CoNPs were isolated by precipitation into hexanes (500 mL), yielding a black powder (yield = 1.53 g) that was soluble in a wide range of organic solvents (*e.g.*, methylene chloride, THF, toluene). The sample for TEM analysis was prepared by dispersing the isolated powder (1 mg) in toluene (2 mL) *via* sonication for 15 min followed by drop casting onto a carbon-coated Cu grid. The particle size of the PS-CoNPs was determined to be 20 ± 2.4 nm *via* TEM. Magnetic properties of PS-CoNPs were measured using VSM at room temperature: $\mathbf{M}_s$ = 41.2 emu/g, $\mathbf{H}_c$ = 713 Oe; and at 60 K, $\mathbf{M}_s$ = 43.7 emu/g, $\mathbf{H}_c$ = 1440 Oe. TGA analysis showed 41% of organics by mass.

Gram Scale Preparation of PS-Co_3O_4 Nanostructures. Isolated powders of PS-CoNPs (1.36 g) was redispersed in DCB (50 mL) *via* sonication for 15 min. The black solution was charged into a three-neck round-bottom flask equipped with a reflux condenser and a stir bar. The ferrofluid was heated to 175 °C and stirred at 300 rpm, while bubbling with oxygen for a specific period of time. After 1 week of oxidation, the reaction was cooled to room temperature. The ferrofluid was isolated by precipitation into hexanes (500 mL), followed by centrifugation at 5000 rpm for 15 min to yield a black powder (yield = 1.04 g) that was soluble in a wide range of organic solvents (*e.g.*, methylene chloride, THF, toluene). TEM sample was prepared as previously described. The diameter of the PS-cobalt oxide nanowire **3** was determined to be 32 ± 3.5 nm *via* TEM. Magnetic properties of PS-cobalt oxide **3** were measured using VSM at room temperature: **M** = 0.2 emu/g at 10000 Oe; and at 60 K, **M** = 0.38 emu/g at 10000 Oe. TGA analysis showed 11% of organics by mass.

Calcined Cobalt Cobaltite, Co_3O_4 Nanostructures (4). The as-synthesized PS-cobalt oxide nanowire powders **3** were calcined at 400 °C in the furnace for 16 h in air to yield polycrystalline Co_3O_4 nanowires **4** as determined from XRD. The magnetic properties of the calcined powders were measured using VSM at room temperature: **M** = 0.09 emu/g at 10000 Oe; and at 60 K, **M** = 0.25 emu/g at 10000 Oe.

Preparation of Cobalt Oxide Films on ITO. ITO slides were cut and then cleaned with 10% aqueous Triton X-100 solution followed by rinsing and sonication in nanopure (18 MΩ cm) water for 10 min. The ITO was then sonicated in absolute ethanol for 10 min. Once removed from ethanol, the slides were dried under a stream of N_2 and immedately etched with HI (50% aqueous solution). The acid-etched slide was immediately spin coated (1000 rpm) with the nanoparticle dispersion in toluene (c = 25 mg/mL) to obtain thin films of the polymer coated colloids on ITO. Film thickness ranged from 50−60 nm as determined from AFM. The films were then dried under vacuum heating at 70 °C for several hours. For the calcined cobalt oxide film on ITO, a dispersion of polystyrene-coated cobalt oxide was deposited as described previously. Then, the film was heated at 400 °C in air for 16 h.

UV−Visible Absorption Spectroscopy. A dispersion of polystyrene-coated cobalt oxide nanowires was deposited onto ITO and calcined at 400 °C in air as described previously. The UV−vis absorption spectra of the Co_3O_4 film on ITO were recorded using the Agilent UV−visible spectrometer (no. 8453A) and the spectra obtained were analyzed by Chemistation software.

Cyclic Voltammetry Measurements. A potential *versus* current profile for the polymer-coated cobalt nanoparticles and cobalt oxide thin films on ITO were obtained at a sweep rate of 20 mV/s at room temperature in the potential range of 0.8 and −0.9 V *versus* the Ag/AgCl (saturated KCl) in 0.1 M NaOH (aq). The electrolyte solution was purged with argon for 30 min and then transferred into the electrochemical cell *via* syringe prior to cyclic voltammetry experiments.

Acknowledgment. The Office of Naval Research Young Investigator Program (N00014-07-1-0796), Office of Naval Research, NSF Science and Technology Center for Materials and Devices for Information Technology Research (DMR-0120967), and the National Science Foundation (DMR-0645618, CHE-0517963, CHE-0848624) are acknowledged for synthetic support of this research. The Division of Chemical Sciences, Geosciences, and Biosciences, Office of Basic Energy Sciences of the U.S. Department of Energy through Grant DE-FG03-02ER15753 is acknowledged for spectroscopic and electrochemical characterization support of this work. Bryan Korth and Clayton Shallcross are gratefully acknowledged for assistance with FE-SEM imaging and helpful discussions.

Supporting Information Available: Experimental procedures and additional TEM, band gap calculations, and cyclic voltammagram. This material is available free of charge *via* the Internet at http://pubs.acs.org.

REFERENCES AND NOTES

1. Alstrum-Acevedo, J. H.; Brennaman, M. K.; Meyer, T. J. Chemical Approaches to Artificial Photosynthesis. 2. *Inorg. Chem.* **2005**, *44*, 6802–6827.
2. Arico, A. S.; Bruce, P.; Scrosati, S.; Tarascon, J.-M.; Van Schalkwijk, W. Nanostructured Materials for Advanced Energy Conversion and Storage Devices. *Nat. Mater.* **2005**, *4*, 366–377.
3. Kanan, M. W.; Nocera, D. G. *In Situ* Formation of an Oxygen-Evolving Catalyst in Neutral Water Containing Phosphate and Co^{2+}. *Science* **2008**, *321*, 1072–1075.
4. Osterloh, F. Inorganic Materials as Catalysts for Photochemical Splitting of Water. *Chem. Mater.* **2008**, *20*, 35–54.
5. Ryan, J. V.; Berry, A. D.; Anderson, M. L.; Long, J. W.; Stroud, R. M.; Cepak, V. M.; Browning, V. M.; Rolison, D. R.; Merzbacher, C. I. Electronic Connection to the Interior of a Mesoporous Insulator with Nanowires of Crystalline RuO_2. *Nature* **2000**, *406*, 169–172.
6. Long, J. W.; Dunn, B.; Rolison, D. R.; White, H. S. Three Dimensional Battery Architectures. *Chem. Rev.* **2004**, *104*, 4463–4492.
7. Long, J. W.; Rolison, D. R. Architectural Design, Interior Decoration, and Three-Dimensional Plumbing *en Route* to Multifunctional Nanoarchitectures. *Acc. Chem. Res.* **2007**, *40*, 854–862.
8. Alexander, B. D.; Kulesza, P. J.; Rutkowska, I.; Solarskac, R.; Augustynski, J. Metal Oxide Photoanodes for Solar Hydrogen Production. *J. Mater. Chem.* **2008**, *18*, 2298–2303.
9. Estrada, W.; Fantini, M. C. A.; de Castro, S. C.; Polo da Fonseca, C. N.; Gorenstein, A. Radio Frequency Sputtered Cobalt Oxide Coating: Structural, Optical, and Electrochemical Characterization. *J. Appl. Phys.* **1993**, *74*, 5835–5841.
10. Svegl, F.; Orel, B.; Hutchins, M. G.; Kalcher, K. Structural and Spectroelectrochemical Investigations of Sol−Gel Derived Electrochromic Spinel Co_3O_4 Films. *J. Electrochem. Soc.* **1996**, *143* (5), 1532–1539.
11. Poizot, P.; Laruelle, S.; Grugeon, S.; Dupont, L.; Tarascon, J.-M. Nano-Sized Transition-Metal Oxides as Negative-Electrode Materials for Lithium-Ion Batteries. *Nature* **2000**, *407*, 496–499.
12. Li, W.-Y.; Xu, L.-N.; Chen, J. Co_3O_4 Nanomaterials in Lithium-Ion Batteries and Gas Sensors. *Adv. Func. Mater.* **2005**, *15*, 851–857.
13. Li, Y.; Tan, B.; Wu, Y. Freestanding Mesoporous Quasi-Single-Crystalline Co_3O_4 Nanowire Arrays. *J. Am. Chem. Soc.* **2006**, *128*, 14258–14259.
14. Nam, K. T.; Kim, D.-W.; Yoo, P. J.; Chiang, C.-Y.; Meethong, N.; Hammond, P. T.; Chiang, Y.-M.; Belcher, A. M. Virus-Enabled Synthesis and Assembly of Nanowires for Lithium Ion Battery Electrodes. *Science* **2006**, *312*, 885–888.
15. Li, Y.; Tan, B.; Wu, Y. Mesoporous Co_3O_4 Nanowire Arrays for Lithium Ion Batteries With High Capacity and Rate Capability. *Nano Lett.* **2008**, *8*, 265–270.
16. Shim, H.-S.; Shinde, V. R.; Kim, H.-J.; Sung, Y.-E.; Kim, W.-B. Porous Cobalt Oxide Thin Films from Low Temperature Solution Phase Synthesis for Electrochromic Electrode. *Thin Solid Films* **2008**, *516*, 8573–8578.
17. Chen, Y. W. D.; Noufi, R. N. Plating of Nickel and Cobalt Oxides. *J. Electrochem. Soc.* **1984**, *131*, 731–5.
18. Schumacher, L. C.; Holzheuter, I. B.; Hill, I. R.; Dignam, M. J. Semiconducting and Electrocatalytic Properties of Sputtered Cobalt Oxide Films. *Electrochim. Acta* **1990**, *35*, 975–984.
19. Monk, P. M. S.; Chester, S. L.; Higham, D. S.; Partridge, R. D. Electrodeposition of Cobalt Oxide Doped with Additional Metal Oxides. *Electrochim. Acta* **1994**, *39*, 2277–84.
20. Castro, E. B.; Gervasi, C. A.; Vilche, J. R. Oxygen Evolution on Electrodeposited Cobalt Oxides. *J. Appl. Electrochem.* **1998**, *28*, 835–841.
21. Casella, I. G. Electrodeposition of Cobalt Oxide Films from Carbonate Solutions Containing Co(II)−Tartrate Complexes. *J. Electroanal. Chem.* **2002**, *520*, 119–125.
22. Casella, I. G.; Gatta, M. Study of the Electrochemical Deposition and Properties of Cobalt Oxide Species in Citrate Alkaline Solutions. *J. Electroanal. Chem.* **2002**, *534*, 31–38.
23. Mendoza, L.; Albin, V.; Cassir, M.; Galtayries, A. Electrochemical Deposition of Co_3O_4 Thin Layers in Order to Protect the Nickel-Based Molten Carbonate Fuel Cell Cathode. *J. Electroanal. Chem.* **2003**, *548*, 95–107.
24. Spataru, N.; Terashima, C.; Tokuhiro, K.; Sutanto, I.; Tryk, D. A.; Park, S.-M.; Fujishima, A. Electrochemical Behavior of Cobalt Oxide Films Deposited at Conductive Diamond Electrodes. *J. Electrochem. Soc.* **2003**, *150*, E337-E341.
25. Lin, H.; Tang, W.; Kleiman-Shwarsctein, A.; McFarland, E. W. Oxygen Electroreduction on Gold−Cobalt Oxide Binary Nanocluster Catalysts. *J. Electrochem. Soc.* **2008**, *155*, B200–B206.
26. He, T.; Chen, D.; Jiao, X.; Xu, Y.; Gu, Y. Surfactant-Assisted Solvothermal Synthesis of Co_3O_4 Hollow Spheres with Oriented-Aggregation Nanostructures and Tunable Particle Size. *Langmuir* **2004**, *20*, 8404–8408.
27. Kim, J.-W.; Choi, S. H.; Lillehei, P. T.; Chu, S.-H.; King, G. C.; Watt, G. D. Cobalt Oxide Hollow Nanoparticles Derived by Biotemplating. *Chem. Commun.* **2005**, 4101–4103.
28. Hu, J.; Wen, Z.; Wang, Q.; Yao, X.; Zhang, Q.; Zhou, J.; Li, J. Controllable Synthesis and Enhanced Electrochemical Properties of Multifunctional Au core Co3O4 Shell Nanocubes. *J. Phys. Chem. B* **2006**, *110*, 24305–24310.
29. Ohnishi, M.; Kozuka, Y.; Ye, Q.-L.; Yoshikawa, H.; Awaga, K.; Matsuno, R.; Kobayashi, M.; Takahara, A.; Yokoyama, T.; Bandow, S.; Iijima, S. Phase Selective Preparations and Surface Modifications of Spherical Hollow Nanomagnets. *J. Mater. Chem.* **2006**, *16*, 3215–3220.
30. Titirici, M.-M.; Antonietti, M.; Thomas, A. A Generalized Synthesis of Metal Oxide Hollow Spheres Using a Hydrothermal Approach. *Chem. Mater.* **2006**, *18*, 3808–3812.
31. Chen, Y.; Zhang, Y.; Fu, S. Synthesis and Characterization of Co_3O_4 Hollow Spheres. *Mater. Lett.* **2007**, *61*, 701–705.
32. Du, N.; Zhang, H.; Chen, B.; Wu, J.; Ma, X.; Liu, Z.; Zhang, Y.; Yang, D.; Huang, X.; Tu, J. Porous Co_3O_4 Nanotubes Derived from $Co_4(CO)_{12}$ Clusters on Carbon Nanotube Templates: A Highly Efficient Material for Li Battery Applications. *Adv. Mater.* **2007**, *19*, 4505–4509.
33. Chen, C.-H.; Abbas, S. F.; Morey, A.; Sithambaram, S.; Xu, L.-P.; Garces, H. F.; Hines, W. A.; Suib, S. L. Controlled Synthesis of Self-Assembled Metal Oxide Hollow Spheres *via* Tuning Redox Potentials: Versatile Nanostructured Cobalt Oxides. *Adv. Mater.* **2008**, *20*, 1205–1209.
34. Chernavskii, P. A.; Pankina, G. V.; Zaikovskii, V. I.; Peskov, N. V.; Afanasiev, P. Formation of Hollow Spheres Upon Oxidation of Supported Cobalt Nanoparticles. *J. Phys. Chem. C* **2008**, *112*, 9573–9578.
35. Teng, F.; Xu, T.; Liang, S.; Buergen, G.; Yao, W.; Zhu, Y. Synthesis of Hollow Mn_3O_4-in- Co_3O_4 Magnetic Microspheres and its Chemiluminescence and Catalytic Properties. *Catal. Commun.* **2008**, *9*, 1119–1124.
36. Teng, F.; Yao, W.; Zheng, Y.; Ma, Y.; Xu, T.; Gao, G.; Liang, S.; Teng, Y.; Zhu, Y. Facile Synthesis of Hollow Co_3O_4 Microspheres and its Use as a Rapid Responsive CL Sensor of Combustible Gases. *Talanta* **2008**, *76*, 1058–1064.
37. Tian, L.; Yang, X.; Lu, P.; Williams, I. D.; Wang, C.; Ou, S.; Liang, C.; Wu, M. Hollow Single-Crystal Spinel Nanocubes: The Case of Zinc Cobalt Oxide Grown by a Unique Kirkendall Effect. *Inorg. Chem.* **2008**, *47*, 5522–5524.
38. Zhao, W.; Liu, Y.; Li, H.; Zhang, X. Preparation and Characterization of Hollow Co_3O_4Spheres. *Mater. Lett.* **2008**, *62*, 772–774.
39. Chen, Y.; Hu, L.; Wang, M.; Min, Y.; Zhang, Y. Self-assembled Co_3O_4 Porous Nanostructures and Their Photocatalytic Activity. *Colloids Surf., A* **2009**, *336*, 64–68.
40. Park, J.; Shen, X.; Wang, G. Solvothermal Synthesis and Gas-Sensing Performance of Co_3O_4 Hollow Nanospheres. *Sens. Actuators, B* **2009**, *B136*, 494–498.

41. Salabas, E. L.; Rumplecker, A.; Kleitz, F.; Radu, F.; Schueth, F. Exchange Anisotropy in Nanocasted Co_3O_4 Nanowires. *Nano Lett.* **2006**, *6*, 2977–2981.
42. Rumplecker, A.; Kleitz, F.; Salabas, E.-L.; Schueth, F. Hard Templating Pathways for the Synthesis of Nanostructured Porous Co_3O_4. *Chem. Mater.* **2007**, *19*, 485–496.
43. Shaju, K. M.; Jiao, F.; Debart, A.; Bruce, P. G. Mesoporous and Nanowire Co_3O_4 as Negative Electrodes for Rechargeable Lithium Batteries. *Phys. Chem. Chem. Phys.* **2007**, *9*, 1837–1842.
44. Tueysuez, H.; Comotti, M.; Schueth, F. Ordered Mesoporous Co_3O_4 as Highly Active Catalyst for Low Temperature CO Oxidation. *Chem. Commun.* **2008**, 4022–4024.
45. Tueysuez, H.; Liu, Y.; Weidenthaler, C.; Schueth, F. Pseudomorphic Transformation of Highly Ordered Mesoporous Co_3O_4 to CoO *via* Reduction with Glycerol. *J. Am. Chem. Soc.* **2008**, *130*, 14108–14110.
46. Dong, Z.; Fu, Y.; Han, Q.; Xu, Y.; Zhang, H. Synthesis and Physical Properties of Co_3O_4 Nanowires. *J. Phys. Chem. C* **2007**, *111*, 18475–18478.
47. Du, J.; Chai, L.; Wang, G.; Li, K.; Qian, Y. Controlled Synthesis of One-Dimensional Single-Crystal Co_3O_4 Nanowires. *Aust. J. Chem.* **2008**, *61*, 153–158.
48. Zhang, H.; Wu, J.; Zhai, C.; Ma, X.; Du, N.; Tu, J.; Yang, D. From Cobalt Nitrate Carbonate Hydroxide Hydrate Nanowires to Porous Co_3O_4 Nanorods for High Performance Lithium Ion Battery Electrodes. *Nanotechnology* **2008**, *19*, 035711/1−035711/5.
49. An, K.; Lee, N.; Park, J.; Kim, S.; Hwang, Y.; Park, J.; Kim, J.; Park, J.; Han, M. J.; Yu, J.; Hyeon, T. Synthesis, Characterization, and Self-Assembly of Pencil-Shaped CoO Nanorods. *J. Am. Chem. Soc.* **2004**, *128*, 9753–9760.
50. Guan, H.; Shao, C.; Wen, S.; Chen, B.; Gong, J.; Yang, X. A Novel Method for Preparing Co_3O_4 Nanofibers by Using Electrospun PVA/Cobalt Acetate Composite Fibers as Precursor. *Mater. Chem. Phys.* **2003**, *82*, 1002–1006.
51. Barakat, N. A. M.; Khil, M. S.; Sheikh, F. A.; Kim, H. Y. Synthesis and Optical Properties of Two Cobalt Oxides (CoO and Co_3O_4) Nanofibers Produced by Electrospinning Process. *J. Phys. Chem. C* **2008**, *112*, 12225–12233.
52. Gu, Y.; Jian, F.; Wang, X. Synthesis and Characterization of Nanostructured Co_3O_4 Fibers Used as Anode Materials for Lithium Ion Batteries. *Thin Solid Films* **2008**, *517*, 652–655.
53. Redl, F. X.; Cho, K.-S.; Murray, C. B.; O'Brien, S. Three-Dimensional Binary Superlattices of Magnetic Nanocrystals and Semiconductor Quantum Dots. *Nature* **2003**, *423*, 968–971.
54. Manoharan, V. M.; Elsesser, M. T.; Pine, D. J. Dense Packing and Symmetry in Small Clusters of Microspheres. *Science* **2003**, *301*, 483–487.
55. Park, S.; Lim, J.-H.; Chung, S.-W.; Mirkin, C. A. Self-Assembly of Mesoscopic Metal−Polymer Amphiphiles. *Science* **2004**, *16*, 348–351.
56. Benkoski, J. J.; Bowles, S. E.; Korth, B. D.; Jones, R. A.; Douglas, J. F.; Karim, A.; Pyun, J. Field Induced Formation of Mesoscopic Polymer Chains from Functional Ferromagnetic Nanoparticles. *J. Am. Chem. Soc.* **2007**, *129*, 6291–6297.
57. Benkoski, J. J.; Bowles, S. E.; Jones, R. A.; Douglas, J. F.; Pyun, J.; Karim, A. Self-Assembly of Polymer-Coated Ferromagnetic Nanoparticles into Mesoscopic Polymer Chains and Visualization Using Fossilized Liquid Assembly. *J. Polym. Sci., Part B* **2008**, *46*, 2267–2277.
58. DeVries, G. A.; Brunnbauer, M.; Hu, Y.; Jackson, A. M.; Long, B.; Neltner, B. T.; Uzun, O.; Wunsch, B. H.; Stellacci, F. Divalent Metal Nanoparticles. *Science* **2007**, *315*, 358–361.
59. Carney, R. P.; De Vries, G. A.; Dubois, C.; Kim, H.; Kim, J. Y.; Singh, C.; Ghorai, P. K.; Tracy, J. B.; Stiles, R. L.; Murray, R. W.; *et al.* Size Limitations for the Formation of Ordered Striped Nanoparticles. *J. Am. Chem. Soc.* **2008**, *130*, 798–799.
60. De Vries, G. A.; Talley, F. R.; Carney, R. P.; Stellacci, F. Thermodynamic Study of the Reactivity of the Two Topological Point Defects Present in Mixed Self-Assembled Monolayers on Gold Nanoparticles. *Adv. Mater.* **2008**, *20*, 4243–4247.
61. Nakata, K.; Hu, Y.; Uzun, O.; Bakr, O.; Stellacci, F. Chains of Superparamagnetic Nanoparticles. *Adv. Mater.* **2008**, *20*, 4294–4299.
62. Furst, E. M.; Suzuki, C.; Fermigier, M.; Gast, A. P. Permanently Linked Monodisperse Paramagnetic Chains. *Langmuir* **1998**, *14*, 7334–7336.
63. Biswal, S. L.; Gast, A. P. Mechanics of Semiflexible Chains Formed by Poly(ethylene glycol)-Linked Paramagnetic Particles. *Phys. Rev. E* **2003**, *68*, 021402/1−021402/9.
64. Goubault, C.; Jop, P.; Fermigier, M.; Baudry, J.; Bertrand, E.; Bibette, J. Flexible Magnetic Filaments as Micromechanical Sensors. *Phys. Rev. Lett.* **2003**, *91*, 260802/1–260802/4.
65. Biswal, S. L.; Gast, A. P. Micromixing with Linked Chains of Paramagnetic Particles. *Anal. Chem.* **2004**, *76*, 6448–6455.
66. Biswal, S. L.; Gast, A. P. Rotational Dynamics of Semiflexible Paramagnetic Particle Chains. *Phys. Rev. E* **2004**, *69*, 041406/1−041406/9.
67. Cohen-Tannoudji, L.; Bertrand, E.; Bressy, L.; Goubault, C.; Baudry, J.; Klein, J.; Joanny, J.-F.; Bibette, J. Polymer Bridging Probed by Magnetic Colloids. *Phys. Rev. Lett.* **2005**, *94*, 038301/1−038301/4.
68. Dreyfus, R.; Baudry, J.; Roper, M. L.; Fermigier, M.; Stone, H. A.; Bibette, J. Microscopic Artificial Swimmers. *Nature* **2005**, *437*, 862–865.
69. Goubault, C.; Leal-Calderon, F.; Viovy, J.-L.; Bibette, J. Self-Assembled Magnetic Nanowires Made Irreversible by Polymer Bridging. *Langmuir* **2005**, *21*, 3725–3729.
70. Singh, H.; Laibinis, P. E.; Hatton, T. A. Synthesis of Flexible Magnetic Nanowires of Permanently Linked Core-Shell Magnetic Beads Tethered to a Glass Surface Patterned by Microcontact Printing. *Nano Lett.* **2005**, *5*, 2149–2154.
71. Gao, J.; Zhang, B.; Zhang, X.; Xu, B. Magnetic-Dipolar-Interaction-Induced Self-Assembly Affords Wires of Hollow Nanocrystals of Cobalt Selenide. *Angew. Chem., Int. Ed.* **2006**, *45*, 1220–1223.
72. Pileni, M. P. Self-Assembly of Inorganic Nanocrystal: Fabrication and Collective Intrinsic Properties. *Acc. Chem. Res.* **2007**, *40*, 685–693.
73. Singh, H.; Hatton, T. A. Orientational Dependence of Apparent Magnetic Susceptibilities of Superparamagnetic Nanoparticles inPplanar Structured Arrays: Effect on Magnetic Moments of Nanoparticle-Coated Core-Shell Magnetic Beads. *J. Magn. Magn. Mater.* **2007**, *315*, 53–64.
74. Cohen-Tannoudji, L.; Bertrand, E.; Baudry, J.; Robic, C.; Goubault, C.; Pellissier, M.; Johner, A.; Thalmann, F.; Lee, N. K.; Marques, C. M.; Bibette, J. Measuring the Kinetics of Biomolecular Recognition with Magnetic Colloids. *Phys. Rev. Lett.* **2008**, *100*, 108301/1–108301/4.
75. Zerrouki, D.; Baudry, J.; Pine, D.; Chaikin, P.; Bibette, J. Chiral Colloidal Clusters. *Nature* **2008**, *455*, 380–382.
76. Erb, R. M.; Son, H. S.; Samanta, B.; Rotello, V. M.; Yellen, B. B. Magnetic Assembly of Colloidal Superstructures with Multipole Aymmetry. *Nature* **2009**, *457*, 999–1002.
77. Zhou, Z.; Liu, G.; Han, D. Coating and Structural Locking of Dipolar Chains of Cobalt Nanoparticles. *ACS Nano* **2009**, *3*, 165–172.
78. Bowles, S. E.; Wu, W.; Kowalewski, T.; Schalnat, M. C.; Davis, R. J.; Pemberton, J. E.; Shim, I.; Korth, B. D.; Pyun, J. Magnetic Assembly and Pyrolysis of Functional Ferromagnetic Nanoparticles into One-Dimensional Carbon Nanostructures. *J. Am. Chem. Soc.* **2007**, *129*, 8694–8695.
79. Yin, Y.; Rioux, R. M.; Erdonmez, C. K.; Hughes, S.; Somorjai, G. A.; Alivisatos, A. P. Formation of Hollow Nanocrystals Through the Nanoscale Kirkendall Effect. *Science* **2004**, *304* (5671), 711–714.
80. Yin, Y.; Erdonmez, C. K.; Cabot, A.; Hughes, S.; Alivisatos, A. P. Colloidal Synthesis of Hollow Cobalt Sulfide Nanocrystals. *Adv. Funct. Mater.* **2006**, *16*, 1389–1399.

81. Butter, K.; Bomans, P. H. H.; Frederick, P. M.; Vroege, J.; PhilipseA. P. Direct Observation of Dipolar Chains in Iron Ferrofluids by Cryogenic Electron Microscopy. *Nat. Mater.* **2003**, *2*, 88.
82. Ishida, Y.; Aida, T. Homochiral Supramolecular Polymerization of an "S"-Shaped Chiral Monomer: Translation of Optical Purity Into Molecular Weight Distribution. *J. Am. Chem. Soc.* **2002**, *124*, 14017–14019.
83. Zhao, D.; Moore, J. S. Nucleation-Elongation: A Mechanism for Cooperative Supramolecular Polymerization. *Org. Biomol. Chem.* **2003**, *1*, 3471–3491.
84. Scherman, O. A.; Ligthart, G. B. W. L.; Sijbesma, R. P.; Meijer, E. W. A Selectivity-Driven Supramolecular Polymerization of an AB Monomer. *Angew. Chem., Int. Ed.* **2006**, *45*, 2072–2076.
85. Kumar, A. M. S.; Sivakova, S.; Marchant, R. E.; Rowan, S. J. Surface-Aided Supramolecular Polymerization: A Route to Controlled Nanoscale Assemblies. *Small* **2007**, *3*, 783–787.
86. Hawker, C. J.; Bosman, A. W.; Harth, E. New Polymer Synthesis by Nitroxide Mediated Living Radical Polymerizations. *Chem. Rev.* **2001**, *101*, 3661–3688.
87. Lacroix-Desmazes, P.; Lutz, J. F.; Chauvin, F.; Severac, R.; Boutevin, B. Living Radical Polymerization: Use of an Excess of Nitroxide as a Rate Moderator. *Macromolecules* **2001**, *34*, 8866–8871.
88. Hawker, C. J.; Wooley, K. L. The Convergence of Synthetic Organic and Polymer Chemistries. *Science* **2005**, *309*, 1200–1205.
89. Matyjaszewski, K.; Xia, J. Atom Transfer Radical Polymerization. *Chem. Rev.* **2001**, *101*, 2921–2990.
90. Risbud, A. S.; Snedeker, L. P.; Elcombe, M. M.; Cheetham, A. L.; Seshadri, R. Wurtzite CoO. *Chem. Mater.* **2005**, *17*, 834–838.
91. Makhlouf, S. A. Magnetic Properties of Co_3O_4 Nanoparticles. *J. Magn. Magn. Mater.* **2002**, *246*, 184–190.
92. Windisch, C. F.; Ferris, K.; Exarhos, G. J.; Sharma, S. K. Conducting Spinel Oxide Films with Infrared Transparency. *Thin Solid Films* **2002**, *420*−*421*, 89–99.
93. Langell, M. A.; Anderson, M. D.; Carson, G. A.; Peng, L.; Smith, S. Valence-Band Electronic Structure of Co_3O_4 Epitaxy on CoO(100). *Phys. Rev. B* **1999**, *59*, 4791–4798.
94. Gulino, A.; Fragala, I. Cobalt Hexafluoroacetylacetonate Polyether Adducts for Thin Films of Cobalt Oxides. *Inorg. Chim. Acta* **2005**, *358*, 4466–4472.
95. Barreca, D.; Massign, C.; Daolio, S.; Fabrizio, M.; Piccirillo, C.; Armelao, L.; Tondello, E. Composition and Microstructure of Cobalt Oxide Thin Films Obtained from a Novel Cobalt(II) Precursor by Chemical Vapor Deposition. *Chem. Mater.* **2001**, *13*, 588–593.
96. Gulino, A.; Fiorito, G.; Fragala, I. Deposition of Thin Films of Cobalt Oxides by MOCVD. *J. Mater. Chem.* **2003**, *13*, 861–865.
97. Belova, I. D.; Roginskaya, Y. E.; Shifrina, R. R.; Gagarin, S. G.; Plekhanov, Y. V.; Venevtsev, Y. N. Co(III) Ions High-Spin Configuration in Nonstoichiometric Co_3O_4 Films. *Solid State Commun.* **1983**, *47*, 577–584.
98. Miedzinksa, K. M. E.; Hollebone, B. R.; Cook, J. G. An Assignment of the Optical Absorption Spectrum of Mixed Valence Co_3O_4 Spinel Films. *J. Phys. Chem. Solids* **1987**, *48*, 649.
99. Cox, P. A. *Transition Metal Oxides: An Introduction to their Electronic Structure and Properties*; Clarendon Press: Oxford, U.K., **1992**; p 276.
100. Schlettwein, D.; Hesse, K.; Gruhn, N.; Lee, P. A.; Nebesny, K. W.; Armstrong, N. R. Electronic Energy Levels in Individual Molecules, Thin Films, and Organic Heterojunctions of Substituted Phthalocyanines. *J. Phys. Chem. B* **2001**, *105*, 4791–4800.
101. Rose, A. Space-Charge-Limited Currents in Solids. *Phys. Rev.* **1955**, *97*, 1538.
102. Pourbaix, M. *Atlas of Electrochemical Equilibria in Aqueous Solutions*; Pergamon: London, 1966; p 322−329.
103. Barbero, C.; Planes, G. A.; Miras, M. C. Redox Coupled Ion Exchange in Cobalt Oxide Films. *Electrochem. Commun.* **2001**, *3*, 113–116.
104. Lichusina, S.; Chodosovskaja, A.; Selskis, A.; Leinartas, K.; Miecinskas, P.; Juzeliunas, E. Pseudocapacitive Behavior of Cobalt Oxide Films on Nano-Fibre and Magnetron-Sputtered Substrates. *Chemija* **2008**, *19*, 7–15.
105. Keng, P. Y.; Shim, I.; Korth, B. D.; Douglas, J. F.; Pyun, J. Synthesis and Self-Assembly of Polymer-Coated Ferromagnetic Nanoparticles. *ACS Nano* **2007**, *1*, 279–292.